ADVANCED OPTICAL MATERIALS
www.advopticalmat.de

Anti-Reflective Graded-Index Metasurface with Correlated Disorder for Light Management in Planar Silicon Solar Cells

Prerak Dhawan, Maria Gaudig,* Alexander Sprafke, Peter Piechulla, Ralf B. Wehrspohn, and Carsten Rockstuhl*

Recently, many research efforts have been dedicated to improving light coupling into solar cells and reducing optical losses. Promising candidates regarding scalability include direct nano-structuring of the absorber layer, anti-reflective (AR) coatings, or combining both, e.g., pyramidal textures with a conformal coating. However, many of these methods are either insufficient or infeasible for application in thin solar cells. Moreover, approaches based on directly texturing the silicon interface simultaneously strongly increase surface recombination, thus degrading the electronic properties of the solar cell. To circumvent these issues, conformal graded-index metasurfaces with a correlated positional disorder for light trapping in solar cells are proposed and experimentally demonstrated in this contribution. When considered as a part of a prototypical solar cell geometry, a broadband reduction in reflection is observed that results in photocurrent enhancement. The combined consideration of disorder and conformal graded-index layers outperforms structures containing only one of these components. The computational guidance toward optimized designs promises to adjust the framework to other settings. The possibility for large-scale fabrication of the samples paves the way toward a future generation of supporting photonic structures in solar cells.

1. Introduction

Highly efficient solar cells are a key component of our future energy supply, and their development is a prime societal challenge. High efficiency is particularly important because the available land for the installation of solar cells tends to be a limiting factor in the near future. One contribution to these developments by the optics community has been the development of supporting light management structures that improve light coupling to reduce optical reflection losses and light trapping to maximize absorption.[1–3] Promising candidates regarding scalability include directly nanotexturing the absorber, such as the prominent so-called "black silicon" texture for crystalline silicon (c-Si) solar cells.[4] This texture consists of stochastically arranged nano- to micrometer-sized, tapered Si needles, giving rise to broadband and quasi-omnidirectional strong suppression of back reflection and light trapping close to the $4n^2$ limit.[4,5] However, nanotextures such as black silicon oftentimes degrade the electronic properties of the solar cell. Degradation occurs because nanostructuring the absorber layer not only introduces additional defects through the fabrication process but also through the mere strong increase in surface area, thereby increasing the total number of defect sites.[4,6] These defect states increase the surface recombination current, ultimately reducing the output current and, thus, the efficiency of the solar cell. In a nutshell, while black silicon has excellent optical properties, this does not necessarily translate into increased short-circuit current because of predominant electrical losses. Recent research has shown that applying conformal thin film coatings to passivate the texture electronically can almost fully recover the electrical degradation introduced by the fabrication process. However, since surface area enlargement is intrinsic to texturing the interface, surface recombination will always be higher compared to an untextured interface.[7,8] Therefore, planar interfaces are much more preferred, and dedicated light management strategies using metallic grating structures,[9,10] photonic crystals,[11,12] nanospheres,[13,14] and many more were perceived to yield enhanced broadband absorption enhancement.[15,16]

Metasurfaces with high refractive index nanostructures have demonstrated exceptional broadband antireflection ef-

P. Dhawan, C. Rockstuhl
Institute of Theoretical Solid State Physics
Karlsruhe Institute of Technology
Kaiserstr. 12, 76131 Karlsruhe, Germany
E-mail: prerak.dhawan@kit.edu

M. Gaudig, A. Sprafke, P. Piechulla, R. B. Wehrspohn
Institute of Physics
Martin Luther University Halle-Wittenberg
Heinrich-Damerow-Str. 4, 06120 Halle (Saale), Germany
E-mail: maria.gaudig@physik.uni-halle.de

C. Rockstuhl
Institute of Nanotechnology
Karlsruhe Institute of Technology
Kaiserstr. 12, 76131 Karlsruhe, Germany

The ORCID identification number(s) for the author(s) of this article can be found under https://doi.org/10.1002/adom.202302964

DOI: 10.1002/adom.202302964

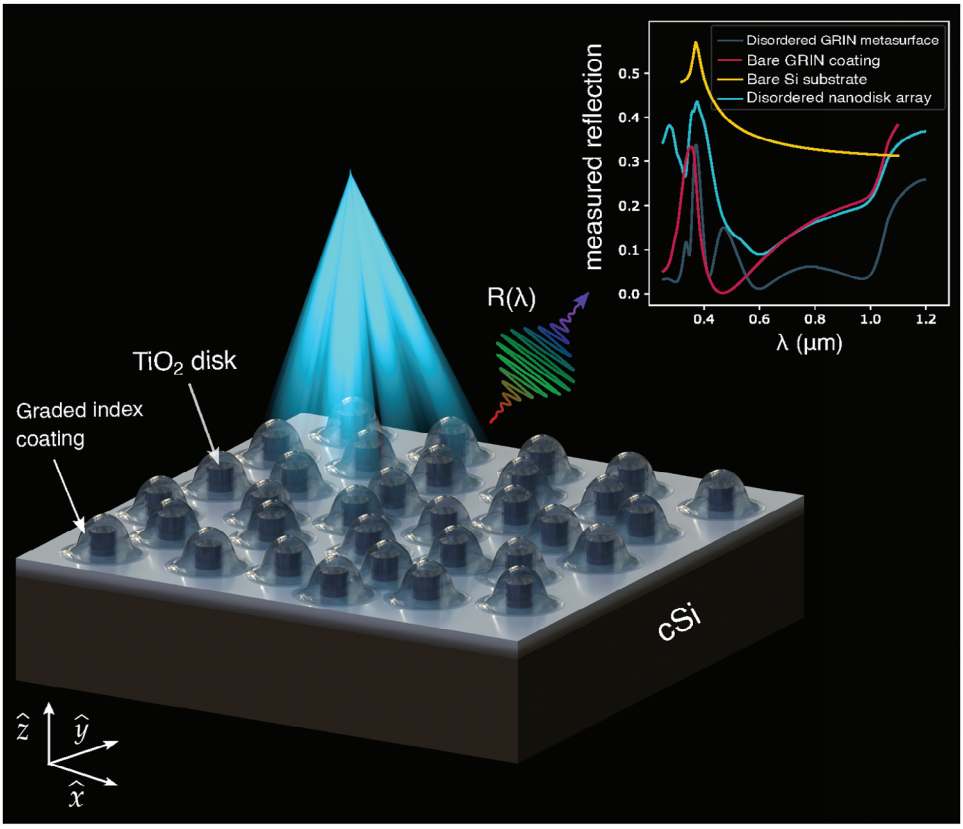

Figure 1. Artistic illustration of the light management structure considered here. The disordered GRIN metasurface consists of dielectric discs arranged in a nearly hyperuniform manner deposited on a polished silicon wafer. Then, a conformal graded-index coating above the disks is achieved by conformal deposition of layers with varying fractions of Al_2O_3 and TiO_2. The inset in the figure compares the reflection from such a device with an unstructured bare GRIN coating, disordered nanodisk array, and a bare Si substrate.

fect in silicon solar cells when arranged in a periodic lattice configuration.[17–20] While such periodic arrangements offer outstanding scattering capabilities by utilizing resonant coupling in the system, the complexity of experimentally realizing periodic structures at industrial length scales remains challenging. This is because periodic metasurfaces often rely on electron-beam lithographic techniques for fabrication. While in perspective, an upscaling is possible using, e.g., nanoimprint techniques, the technology is not yet mature, and there remain technological challenges. Disordered metasurfaces provide a decent trade-off when compared to their periodic counterpart and can use a self-assembly approach for realizing large-scale samples.[21–24]

Recently, an alternative approach was suggested to obtain an all-dielectric graded-index (GRIN) nanostructure integrated on top of an unstructured, i.e., a planar, solar cell.[25] The design involves transformation optics and conformally maps a given texture onto an equivalent structure with a planar interface as an initial step. This procedure allows us to derive a dielectric layer with a spatially inhomogeneous refractive index distribution placed on top of the planar absorber layer that leads to similar scattering features as its textured counterpart. However, this mapping is limited to two dimensions since conformal maps in three dimensions are restricted to inversion, rotation, and translation, which do not capture the desired spatial features needed in the resulting device.[26]

Even though not directly applicable, the structures designed with this approach gave inspiration to their 3D implementation. Two features of the novel top layer can be identified. First, the properties of the original texture responsible for light scattering translated to a spatial distribution of an inhomogeneous material at some spatial frequencies in the lateral direction. Second, reflection suppression translated into a graded-index material in the normal direction. Combined with the ambition to exploit large-scale fabrication techniques for realization, a promising strategy is to identify a technological route to realize structures with these two features while ensuring that the actual design, and even the optimization, is done in the parameter space accessible in the fabrication process.

The state-of-the-art technology we consider here to provide the structuring in the lateral direction is a self-organization process that realizes high-index nanodisks arranged in a nearly hyperuniform disordered pattern on top of the absorber.[27,28] We realize the desired GRIN profile by depositing a GRIN thin-film coating via atomic layer deposition (ALD) in an ultrathin layer-by-layer fashion and varying the refractive index for each layer on top of the disordered pattern. The final disordered GRIN metasurface is illustrated in **Figure 1** with the inset figure showcasing the superior reflectance suppression from one of the fabricated metasurfaces compared to reference structures. Our proposed design circumvents the need for a conformal transformation and reduces

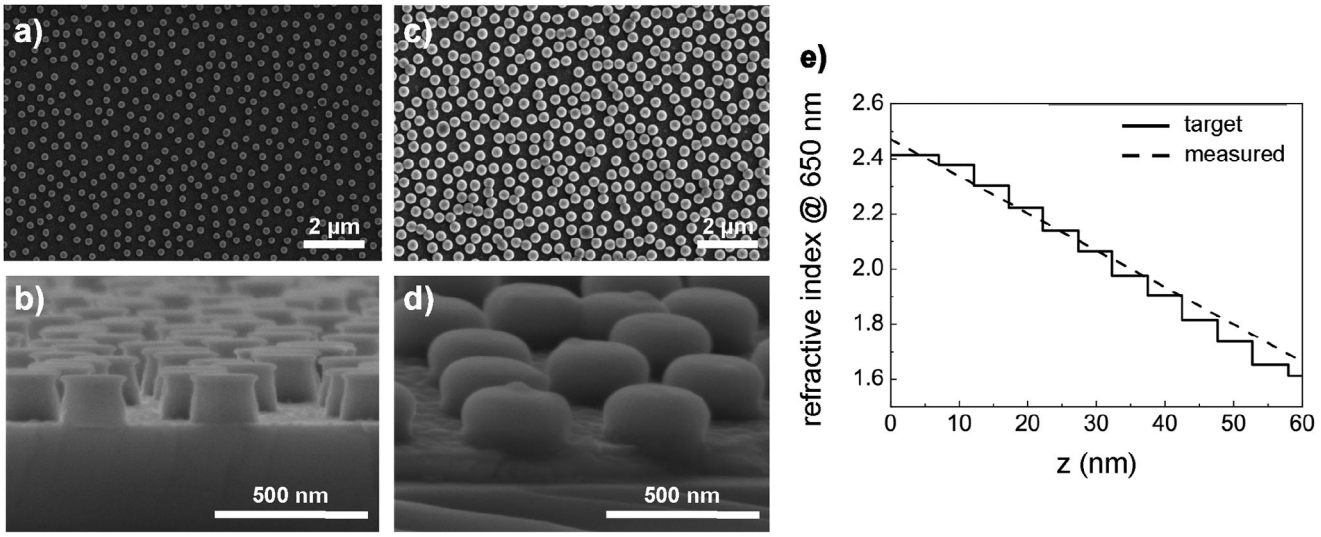

Figure 2. SEM images of nearly hyperuniform disordered TiO_2 nanodisks arrays a,b) and c,d) after deposition of the GRIN film (t = 60 nm), with parameters $[h, d, \bar{d}]$ = [152.5, 235, 461] nm. e) Targeted refractive index profile (solid line) of a planar GRIN coating with t = 60 nm and the corresponding experimentally realized profile measured by spectroscopic ellipsometry (dashed line) at a wavelength of λ = 650 nm.

the problem of finding the optimal nominal geometric features for the metasurface and the graded-index profile covering it. Similar nanostructures with a dielectric thin-film coating have previously been studied in a periodic lattice for their broadband antireflection effect in silicon solar cells.[29,30] However, by considering a disordered arrangement of the scatterers and a smoothly varying index distribution, we largely extend the applicability of such intricate structures.

In this contribution, samples with different geometrical dimensions are fabricated, optically characterized, and compared to simulations. We show that our disordered GRIN metasurface can significantly suppress back reflection and improve light trapping in a c-Si wafer compared to structures that implement only one of the two design strategies. While considered here to perceive a structure that improves the light management in solar cells, other application scenarios will also benefit from such materials.

2. Sample Fabrication Scheme

2.1. Correlated-Disorder TiO_2 Nanodisk Arrays

First, disordered TiO_2 nanodisk arrays are fabricated on commercially available polished 200 µm floatzone silicon wafers (sample area 2 × 3 cm^2) through our previously described self-organized colloid-based nanolithography method.[21,27] This experimental method allows the deterministic variation of the following three structural parameters: disk height h, diameter d, and mean center-to-center distance $\bar{d}$. **Figure** 2a,b shows scanning electron microscopy (SEM) images of fabricated nanodisk arrays on c-Si wafer with parameters $[h, d, \bar{d}]$ = [152.5, 235, 461] nm before depositing the GRIN coating. The TiO_2 disks homogeneously cover the entire surface of the sample in a disordered arrangement with strong spatial correlations, classified as nearly-hyperuniform.[27]

2.2. Graded-Index Layer Deposition

Next, a GRIN coating is applied onto the disordered nanodisk array. For this purpose, we sequentially deposit multiple ultrathin (5 nm) layers, each with a different composition of TiO_2 and Al_2O_3, by ALD.[31,32] The respective composition determines the refractive index of the respective layer, thus enabling a multilayer coating with refractive index adjustable in steps of 5 nm. The highest and lowest indices are fixed by the materials available to our ALD tool, i.e., TiO_2 and Al_2O_3 with $n_{TiO_2} \approx 2.4$ and $n_{Al_2O_3} \approx 1.7$, respectively. This routine allows us to experimentally realize transparent GRIN coatings with arbitrary and virtually smoothly varying index profile along its thickness t with $n_{Al_2O_3} \leq n(t) \leq n_{TiO_2}$.

The index profile of a fabricated planar GRIN coating (t = 60 nm) comprising 12 layers on top of a Si wafer is plotted in Figure 2e. The experimentally realized linear index profile, as analyzed by spectroscopic ellipsometry, and the target index profile agree well and illustrate the congruence between the target and the actual index profile.

By changing the ratio of the deposited materials and the thickness of individual sub-layers, different polynomial index profiles, e.g., quadratic or cubic, can be achieved. Such polynomial profiles are well explored in literature for broadband AR coatings.[33–36] However, for simplicity, we choose to work with a linear profile. Moreover, we suspect that profiles of higher polynomial order will only incrementally change the overall broadband optical response of the final structure, including the nanodisk array. A thickness of t = 60 nm of the GRIN coating is found to be optimal in terms of minimizing broadband reflection of the resulting GRIN metasurface, see discussion below.

GRIN coatings such as in Figure 2e are deposited on the TiO_2 disordered nanodisk arrays, resulting in our disordered GRIN metasurfaces. Figure 2c,d shows SEM images of the final structure after applying a GRIN coating onto the disordered nanodisk arrays shown in Figure 2a,b. In addition to the deposited GRIN

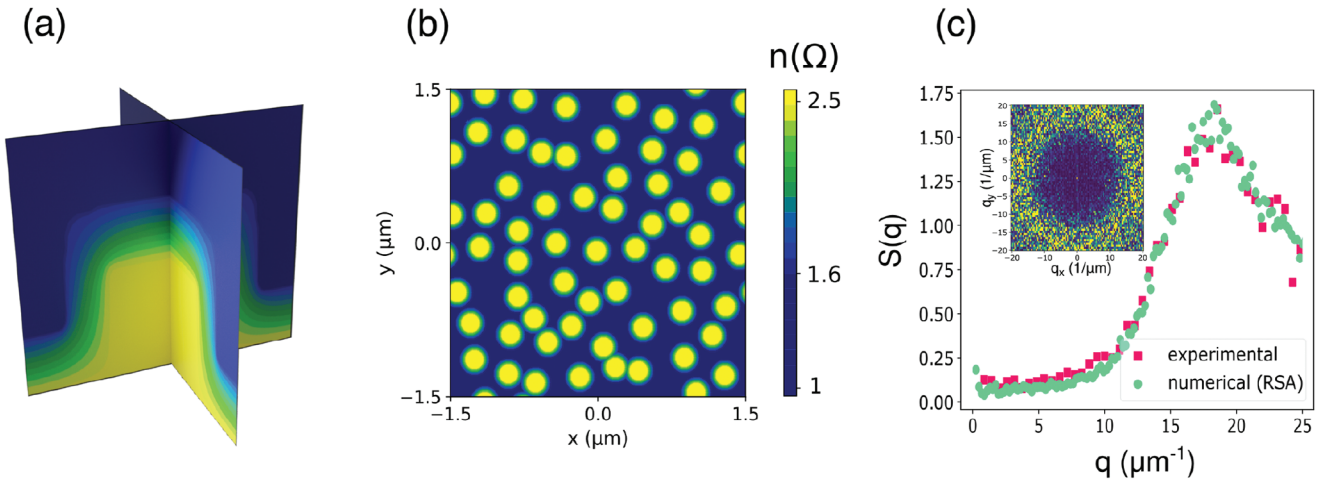

Figure 3. a) Cross-sectional view (*xz*- and *yz*-plane) of the numerically generated structure with a GRIN coating. b) Top view (*xy*-plane) of the disordered array with GRIN coating. c) Angular-averaged structure factor $S(q)$ extracted from experiment compared to $S(q)$ of a simulated sample. The good agreement indicates the correct arrangement of the nanodisks in the simulations. The inset shows experimental $S(\boldsymbol{q})$ for the same sample in 2D.

coating of thickness t in the area between the nanodisks, we find that the radius and height of the overgrown nanodisks have increased by t as well, indicating a successful conformal deposition onto the disordered nanodisk arrays, thus achieving the spatially (vertically and laterally) varying index profile that we aimed for.

3. Theory

3.1. Structural Properties

Cylindrically symmetric scatterers are numerically generated by first obtaining the refractive index distribution of an individual scatterer in the *xz*-plane by solving Laplace's equation in space. Its solution yields the equipotential lines of constant refractive index. Details are given in the Supporting Information. This ensures that each layer is conformally stacked over subsequent layers with gradually varying indices along the normal and lateral directions. Such characteristic features in the inhomogeneous refractive index resemble typical structures obtained using Transformation Optics for wavefront shaping in flat lenses[37,38] and planarized parabolic reflectors,[39,40] and are also essential for light trapping in our proposed structures.[25] The 2D structure is then rotated around the rotation axis of the nanocylinders to achieve a 3D index profile of the scatterer, see **Figure 3**a. Such a design strategy is representative of the experimentally obtained structures described above. This is discussed in detail in the Supporting Information.

To generate a disordered array of scatterers forming the metasurface (Figure 3b), we quantify their arrangement using the structure factor $S(\boldsymbol{q})$ given by

$$S(\boldsymbol{q}) = \frac{1}{N}\left|\sum_{i}^{N} e^{-i\boldsymbol{q}\cdot\mathbf{r}_i}\right|^2 \tag{1}$$

where $\mathbf{r}_i$ is the center position of the i-th scatterer among the other N scatterers while $\boldsymbol{q}$ represents reciprocal space vectors. To account for the statistics of disordered scattering interfaces, we generate a sufficiently large computation of sample area 30 μm × 30 μm. The disordered arrangement for the sample is obtained using a modified Random Sequential Adsorption (RSA) process.[27] Figure 3c plots its angular averaged structure factor $S(q = |\boldsymbol{q}|)$ (cyan circles). The numerically generated structure factor is compared with its experimental counterpart (pink squares). We use in-house image-processing for extracting the particle centers from the SEM images (field-of-view 80 μm × 80 μm) of fabricated samples, and then its structure factor $S(\boldsymbol{q})$. Based on the good agreement in the structure factors, we find that numerically generated disordered arrays statistically correspond well with our experimentally achieved ones. However, since systematic simulations of metasurface layer-stacks with cross-sectional areas as large as, e.g., 30 μm × 30 μm or greater, are demanding, we employ a recently published approach that allows us to use much smaller supercells for anti-reflection and light trapping in solar cells.[41] These small supercells are obtained using the collective coordinate method (CCM).[21,41,42] In short, we could show that using even a single CCM-optimized supercell as a standalone simulation object for ensemble averages or a large-scale sample could reliably predict the optical response of large-scale disordered systems with the benefit of significantly reduced computational effort. The particle distribution shown in Figure 3b uses the structure factor obtained for the large sample (shown in Figure 3c) as a target for realizing CCM samples of cross-section 3 μm × 3 μm. These are later used for an FDTD simulation. To get a final material distribution for the disordered GRIN metasurface that can be considered in the simulations, each lattice coordinate is decorated with the previously identified refractive index distribution for an individual cylinder. More details are given in the Supporting Information.

3.2. Parameter Optimization

Height h, diameter d, and mean distance $\bar{d}$ of the nanodisks, as well as GRIN coating thickness t, are our experimentally accessible degrees of freedom to optimize the light management prop-

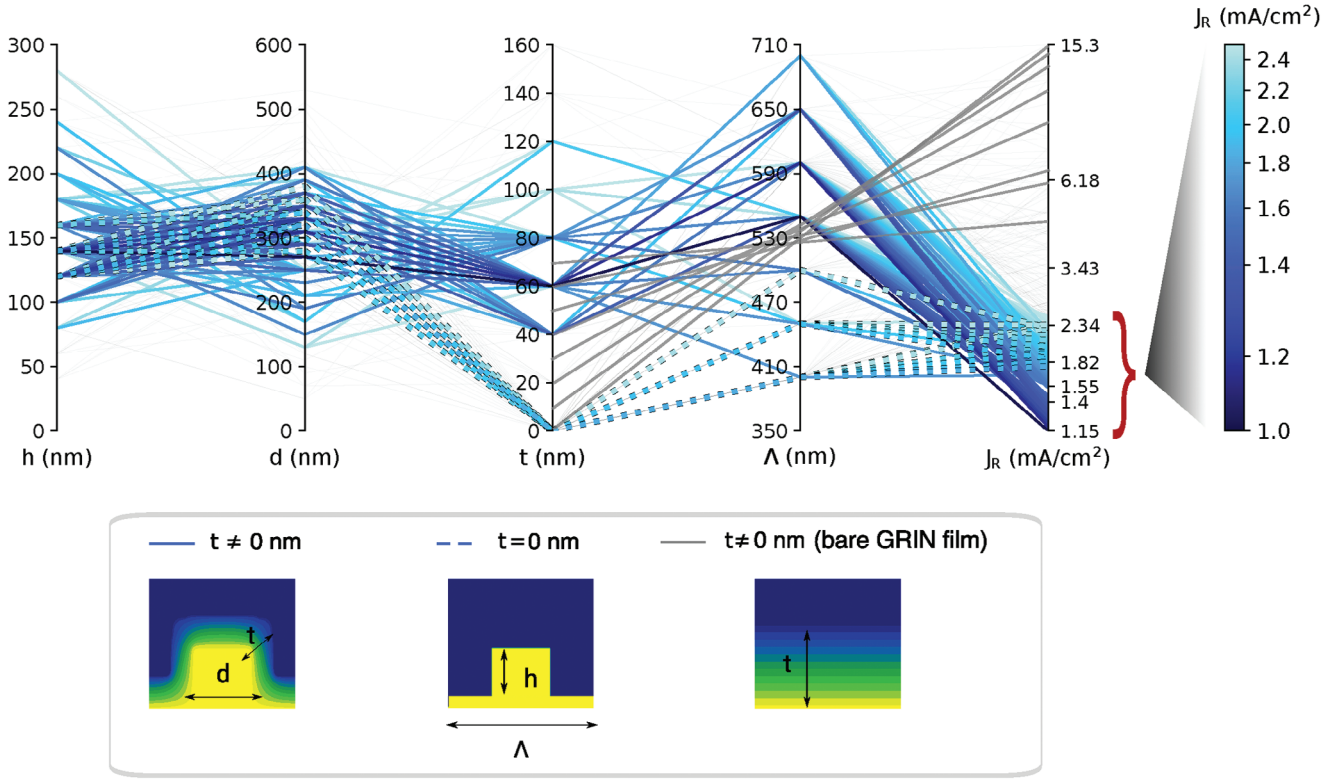

Figure 4. Parallel-coordinate representation of the optimization for minimizing reflected photocurrent J_R as a function of geometric parameters $\mathbf{P} = [h, d, t, \Lambda]$. Solid lines (colored and light gray) depict complete GRIN metasurfaces, dashed lines depict bare nanodisk arrays without GRIN coating, and solid dark gray lines depict bare GRIN coatings without nanodisks. Additionally, the colored lines represent parameter sets **P** for which broadband reflection is suppressed below $J_R = 2.5$ mA/cm^2.

erties of the disordered GRIN metasurfaces. We rely on a slightly simpler system to find a set of starting values that will serve as the target for fabrication. We choose the periodic case (square lattice with pitch Λ) to find optimal parameters since disordered geometries have considerably longer simulation runtimes, which is especially undesirable when considering multidimensional parameter runs. That periodic structure is called the GRIN metasurface. Furthermore, since our fabricated samples possess nearly hyperuniform disorder, the scattering response of the periodic case will be representative for the disordered case in the long-wavelength limit due to a vanishing structure factor for small q's.[43]

The objective function to be minimized is the reflected photocurrent J_R given as,

$$J_R(\mathbf{P}) = e \int_{320\text{nm}}^{1100\text{nm}} \Phi_{AM1.5G}(\lambda)\Phi(\mathbf{P}, \lambda)d\lambda \quad (2)$$

where $\Phi_{AM1.5G}$ is the solar global standard irradiation spectrum, and $\Phi(\mathbf{P}, \lambda) = R(\mathbf{P}, \lambda)$ is the reflection spectrum for a parameter set $\mathbf{P} = [h, d, t, \Lambda]$. We perform a hyperparameter optimization to achieve insights on strong performing (low J_R) **P**'s.[44] The results are summarized in **Figure 4** in a parallel-coordinates plot. Due to the nature of such an optimization problem, it is essential to distinguish the parameter space when the complete GRIN metasurface is considered from the parameter space when it is not, i.e., we also consider the bare nanodisk array without GRIN coating as well as the planar GRIN coating without nanodisks. This guarantees striving for the optimum in each of these settings, a prerequisite for a fair assessment of the benefits when combining nanodisks and GRIN coating to form a GRIN metasurface. In Figure 4, we distinguish the different cases by using different line styles, see figure caption and inset. Moreover, **P**'s with rather small reflection losses ($J_R < 2.5$ mA/cm^2) are colored, while all others ($J_R > 2.5$ mA/cm^2) are (light) gray. The former are chosen for the experimental sample fabrication.

Optimized (periodic) GRIN metasurfaces outperform uncoated nanodisk arrays as well as bare planar GRIN coatings, the minimal reflection currents are $J_R = 1.15$ mA/cm^2, $J_R = 1.80$ mA/cm^2, and $J_R = 4.26$ mA/cm^2, respectively. Comparing the trajectories of high-performing GRIN metasurfaces (colored solid lines) with high-performing uncoated nanodisk arrays (colored dashed lines), we observe that adding the GRIN coating leads to a lower sensitivity of J_R on the remaining parameters, i.e., h, d, and Λ. Only a narrow range of **P**'s with $t = 0$ nm (no GRIN coating) yield J_R's comparable to the case achieved with GRIN coating of any given t.

This indicates that adding the conformal GRIN coating relaxes the requirements of very fine-tuned nanodisk filling fractions and heights. Indeed, we can confirm this trend when extending our studies to include disorder, see discussion below.

Concerning bare GRIN coatings (dark gray full lines), it is evident that for continuously increasing the thickness beyond the largest value shown here (t = 70 nm), lower J_R's may be obtained. However, as we observe in the experiment (see below),

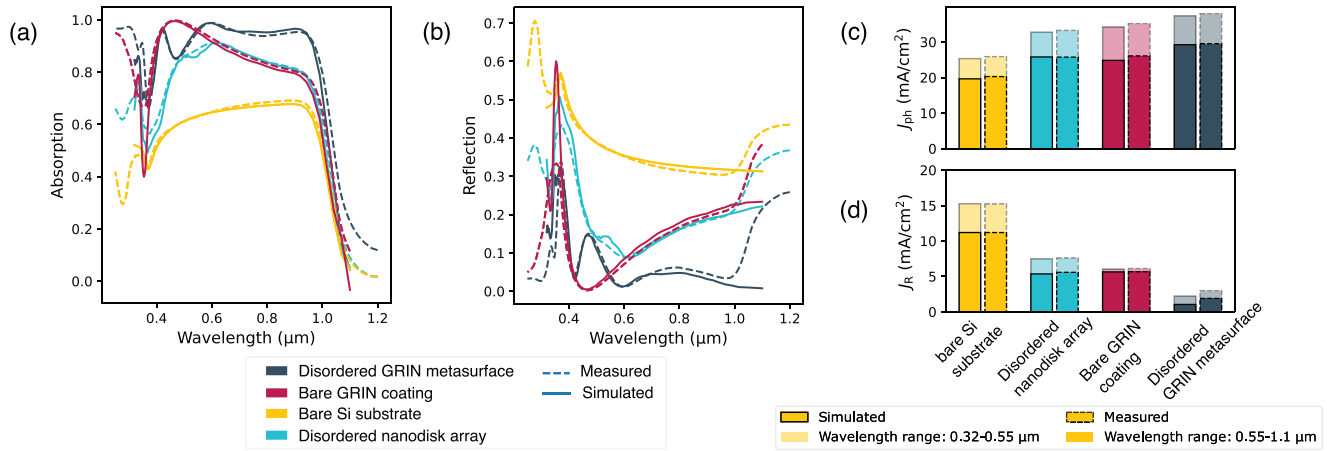

Figure 5. Experimental and simulated a) absorption and b) reflection spectra of a disordered GRIN metasurface with $\mathbf{P} = [153, 234, 60, 461]$ nm and the corresponding disordered bare nanodisk array, the bare GRIN coating and a bare Si substrate. c) Reflected and d) absorbed photocurrents J_R and J_{ph} for the same sample evaluated in different spectral regions, respectively. The solid and dashed lines for each subfigure correspond to the experimentally measured and simulated results, respectively.

this will not necessarily amount to an increased useful absorbed photocurrent since planar structures cannot couple to any scattering/diffraction channels, which is essential for enhanced absorption in the near-infrared spectral range.[45,46]

The optimal parameter sets **P** of GRIN metasurfaces and bare nanodisks are obviously different, in particular, we note that adding the GRIN coating shifts the optimal pitch from $\Lambda = 0.4$ μm to $\Lambda = 0.55$ μm. However, the filling fraction, given by $\mathrm{FF} = \pi(d + 2t)^2/4\Lambda^2$, remains comparable if not strictly equal. This emphasizes that the superior response of nanodisks combined with GRIN coating cannot be trivially reproduced by nanodisks of the same pitch.

3.3. Optical Response of Disordered GRIN Metasurfaces

The insights from the aforementioned parametric optimization are directly fed into the experimental fabrication as target parameters. Since we fabricate disordered nanodisk arrays instead of periodic ones, the mean nanodisk distance $\bar{d}$ is given by the pitch Λ, which will ensure similar scattering features in reciprocal space.

Additionally, we perform full-wave simulations of the disordered structures. Once obtained, the disordered GRIN metasurface is then placed on an air–c-Si interface for a plane-wave illumination from above at normal incidence. Reflectance from that interface and absorption in the c-Si wafer are calculated as the primary quantities. We assume a 200 μm thick c-Si wafer and single-pass propagation of transmitted diffraction orders to calculate absorption. The absorbed photocurrent J_{ph} and the reflected photocurrent J_R for the disordered samples are evaluated using Equation 2 with $\Phi(\mathbf{P})$ being the absorption or the reflected spectrum for the given geometric parameters $\mathbf{P} = [h, d, t, \bar{d}]$, respectively. Dispersive material properties are taken from experimental measurements and are discussed in the Experimental Section.

4. Results and Discussion

In **Figure 5**, we show the experimental optical response of our best-performing disordered GRIN metasurface, with $\mathbf{P} = [h = 153, d = 234, t = 60, \bar{d} = 461]$ nm, along with numerical simulations. Additionally, the response of the disordered nanodisk array, so before applying the GRIN coating, the bare GRIN coating, and the bare c-Si wafer are plotted.

As expected, a GRIN coating increases the absorption in the c-Si wafer and effectively suppresses back reflection, as shown in Figure 5a,b. Almost trivially, this is the case for a planar Si interface (yellow and magenta data) but accounts also for the structured case (cyan and dark blue data) for which the disordered GRIN metasurface can not only increase the absorption at short wavelengths, as is the case with bare GRIN coating, but also at longer wavelengths. This holds for the fabricated samples as well as for the numerical results. This can also be seen quantitatively in Figure 5c,d where the absorbed and reflected photocurrents J_R and J_{ph}, respectively, calculated using Equation (2) are decomposed into the contributions from the short and long spectral range. Measured reflectance, absorbance, and the corresponding photocurrents contain all the major features predicted by the simulations, indicating the accuracy of our numerical approach. Noticeable deviations from the simulations are only observed for $\lambda > 1$ μm where the measured reflectance increases for all samples due to rear side reflection. This was not accounted for in the simulations. Consequently, this increases the absorption in the wafer beyond the single-pass absorption. Thus, the measured absorption is greater than the simulated. For the wavelength range 0.32–0.55 μm, the individual scattering elements contribute more to the overall response than their arrangement statistics for $\bar{d} = 461$ nm, due to the wavelength range being comparable to the mean interparticle distance. The current densities (absorbed and reflected) of the fabricated samples agree well with the simulations, thus indicating the mean height and diameter of the deposited nanodisks and thickness of the gradient layer coating match well with the simulations. The anti-reflective features of the graded-index are most intuitive in this spectral region, as the smooth variation in the refractive index decreases the impedance mismatch between air and c-Si. Due to the short absorption depth of silicon (<2 μm) in this spectral range, enhanced light incoupling is sufficient to increase absorption, as

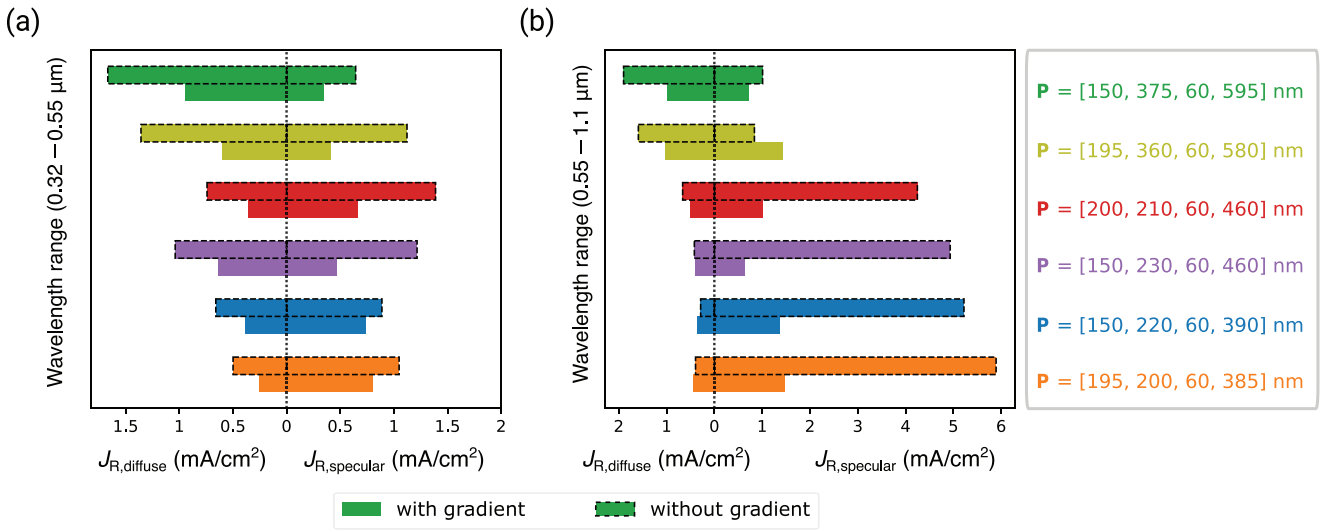

Figure 6. Decomposition of reflection losses J_R of disordered GRIN metasurfaces and bare disordered nanodisk arrays for a) the wavelength range 0.32–0.55 μm and b) (0.55–1.1 μm). For each subfigure, the left-side bars represent contributions of diffused reflection, whereas the right-side bars represent contributions of specular reflection. Each color represents a sample with different geometric parameters given by $P = [h, d, t, \bar{d}]$. The solid and dashed bounding boxes indicate structures with and without the graded-index coating, respectively.

can be seen by the light-colored bar plots for bare GRIN coating and disordered GRIN metasurface (shown in magenta and dark-blue respectively).

For the wavelength range 0.55–1.1 μm, where the presence of correlated disorder influences overall scattering, the current densities of the fabricated disordered metasurface also correspond well with the simulations, indicating that the particle statistics from the experiments align closely with the simulated data.

The superior optical properties of our disordered GRIN metasurface can be understood when considering not just one such fabricated sample but rather multiple samples with different parameters. **Figure 6** summarizes these properties for multiple parameter sets by decomposing the reflected photocurrent of the simulated nanodisk samples into its specular and diffused components for different spectral regions.

For the wavelength range 0.32–0.55 μm, diffused back reflection starts to dominate the overall scattering for increasing interparticle distance. This is indicated by larger $J_{R,\,diffuse}$ in comparison to $J_{R,\,specular}$ for increasing $\bar{d}$ from bottom to top in Figure 6a. In this spectral region, the wavelength is comparable to the mean-interparticle distance as well as the height and diameter of the scatterers. The contribution to the diffused back reflection is then due to large individual scatterer response as well as their disordered arrangement (large $S(\boldsymbol{q})$ for $q \approx 2\pi/\bar{d}$, as shown in Figure 3c. While good suppression of reflection for $\lambda < 0.45$ μm can already occur from having a smoothly varying refractive index along the normal direction, reflection suppression for $0.45\ \mu m \leqslant \lambda < 0.55$ μm depends on having features along the lateral direction, like the dielectric nanodisks in the sample, as they are well-known to preferentially scatter light due to their ability to manipulate multipolar Mie resonances in a broadband manner by tuning their geometrical parameters.[17,47] These lateral features also have a strong light trapping effect, as they yield a greater absorption when compared to a bare GRIN coating by exciting higher diffraction orders in the absorbing layer that have a longer optical path length. The disordered GRIN metasurface capitalizes on both aspects by having conformally varying index along both normal and lateral directions above the disordered nanodisks. Consequently, the reflectance of the disordered GRIN metasurface in this spectral region (shown in Figure 6a) is reduced from both specular and diffused components. This reduction extends beyond what is observed in its bare disordered nanodisk counterpart and holds for all the geometric parameters in Figure 6. This observation is consistent with the light trapping effect obtained from a spatially inhomogeneous material distribution obtained from conformal transformation optics.[25]

In contrast, for 0.55–1.1 μm, where the lateral features are not resolved by the incident wavelength, backscattering is limited to only small angles due to $S(\boldsymbol{q} \to 0) = 0$ for nearly hyperuniform particle arrangement, as evident in Figure 3c. In other words, suppressed long-wavelength density fluctuations of the sample allow the system to act as an effectively homogeneous medium, with ideally no diffused backscattering, thus explaining the specular contribution $J_{R,\,specular}$ overpowering the diffused one $J_{R,\,diffused}$.[43] This trend is equally applicable to the disordered GRIN metasurface. Such a response is not expected either from a bare GRIN coating of similar thickness as it will act as a perfect in-coupler at shorter wavelengths but will lose out on this advantage in the longer wavelength range due to increased reflection, or from the bare nanodisks as explained earlier. The disordered GRIN metasurface clearly utilizes the advantageous properties of both the disordered nanodisk array and the GRIN coating by acting as an efficient anti-reflective structure at short as well as long wavelengths and, at the same time, as an efficient light trapping structure at long wavelengths.

To gain a better insight into how the geometric parameters influence the overall performance of the disordered GRIN metasurface, we fabricate multiple such metasurfaces with varying geometrical parameters and compare their optical response with simulations. The aggregated results in **Figure 7** show the pho-

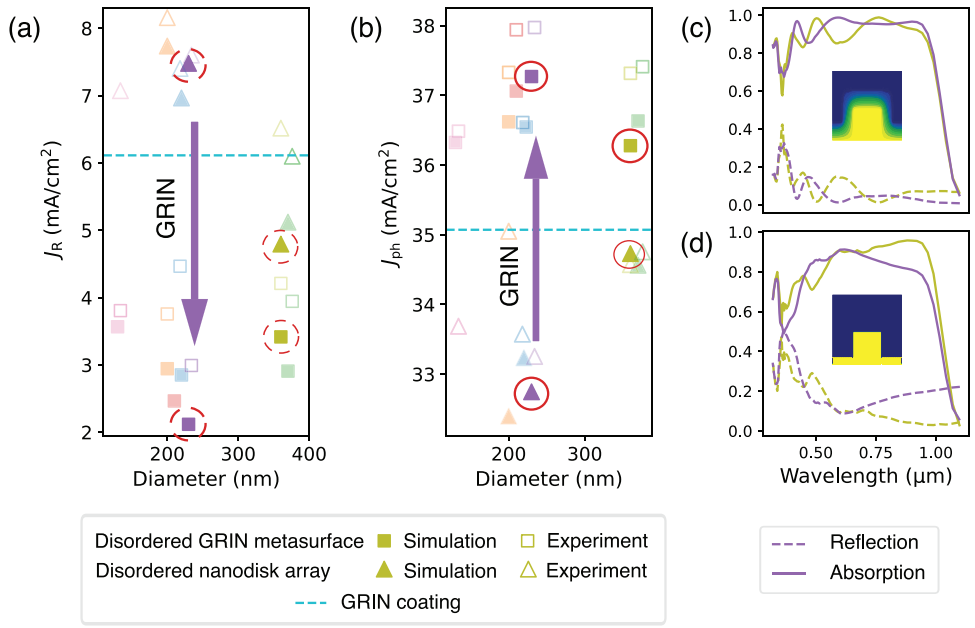

Figure 7. a) Reflected and b) absorbed photocurrent of samples for varying height, diameter, and particle density of the nanodisks. For simplicity, only the variation in diameter is shown here. The empty and filled markers represent results from the experiments and simulations, respectively. The absorbed and reflected photocurrent were evaluated in the wavelength range [0.32−1.1] μm. c) Wavelength-dependent simulated absorbance and reflectance spectrum represented by purple and olive green data points in (a) and (b) from a disordered GRIN metasurface with parameters, $\mathbf{P} = [153, 234, 60, 461]$ nm and $\mathbf{P}' = [195, 361, 60, 577]$ nm, respectively. d) Spectra with the same parameters as in (c) but with $t = 0$ nm

tocurrent for all the samples fabricated with and without a GRIN coating ($t = 60$ nm). Height (50 nm $\leqslant h \leqslant$ 210 nm), diameter (130 nm $\leqslant d \leqslant$ 370 nm), and mean distance (240 nm $\leq \bar{d} \leq$ 600 nm) are varied. However, for simplicity, we only show the variation in diameter. This choice of parameters is well-justified by the findings of Figure 4, considering near-optimal reflectance for its periodic counterpart. Each solid marker of a given color in the figure represents a simulated sample with unique **P**, while the outlined marker of the same color represents the experimental value extracted from optical measurement. For better readability, we only highlight the samples with red circled markers, while faint colors represent the other samples. We see a reasonable agreement between experimentally measured spectra and simulated spectra for structures with and without the graded-index layer, not only for a single fabricated sample but for a wide range of parameter variations. As prompted by the periodic simulations, the optical response is expected to depend on these geometrical parameters sensitively, and, therefore, it is only expected to become more prominent when considering disordered systems. However, a better agreement is generally seen for structures with the graded-index coating, as the conformally varying index relaxes the constraint of precisely extracting every geometrical detail from a fairly large SEM image of the experiment.

While the disordered nanodisk array performs comparably to the bare GRIN coating for a few parametric values only, our proposed disordered GRIN metasurface consistently outperforms both alternative strategies for all considered parameter combinations. This indicates robustness to small geometric variations and was already alluded to in the periodic simulations described above. We find the best performing sample for the GRIN metasurface, as shown in Figure 7 by purple markers (and shown in Figure 5), to increase J_{ph} in the c-Si by 14% and 47% when compared to disordered nanodisk array and bare Si substrate, respectively. Likewise, J_R decreases by 66% and 83% when compared to disordered nanodisk array and bare Si substrate, respectively.

Figure 7c,d elaborates on how our proposed structures are nearly immune to minor geometric changes by comparing two different devices with parameters $\mathbf{P} = [153, 234, 60, 461]$ nm (shown with purple) and $\mathbf{P}' = [195, 361, 60, 577]$ nm (shown with olive green) in the top figure and their respective structures with $t = 0$ nm in the bottom figure. While the cumulative current-loss and the photocurrent for the purple and olive devices are comparable for the disordered GRIN metasurface, the same samples for the disordered nanodisk array have larger differences. This difference can be seen in the absorption and reflection spectra where the purple and olive samples for disordered nanodisk array clearly possess different scattering features. The olive structure has a pronounced reflection around $\lambda \approx 0.5$ μm due to the diffused contribution as this length-scale is smaller than its mean-interparticle distance and a suppressed specular (and diffused) reflection in the long-wavelength range. In contrast, the purple structure predominantly has specular contribution beyond $\lambda \geq \bar{d} = 0.46$ μm with a pronounced increase at longer wavelengths. For the disordered GRIN metasurface, the olive green and the purple samples possess similar scattering features since both can suppress specular and diffused reflection broadband. Obviously, and similar to the disordered nanodisk array, the only notable discrepancy is due to the shifted peak in the olive green sample, which is attributed to a larger mean interparticle distance for the sample. The periodic optimization can then serve as an informed guess for first finding the range wherein most of the disordered GRIN metasurface will possess the superior broadband optical

response and later using this range for fabricating any sample with the disordered arrangement within this parametric range.

5. Conclusion

We suggest equipping a dielectric nanodisk array of strongly correlated disorder with a GRIN coating for superior broadband reflection suppression and simultaneous absorption enhancement in c-Si solar cells. The design parametrization for the gradient index was inspired by transformation optics owing to the smooth spatial variations in its resulting refractive index profile and from the current technological state of the art. The devices are realized with cutting-edge techniques for conformal thin-film deposition and validated using full-wave simulations. Due to the conformal variation in the refractive index distribution, these structures offer much lower reflection loss by suppressing specular and diffused scattering throughout the spectral range of interest. Furthermore, adding the GRIN coating relaxes the constraints of fine-tuned geometric parameters of the nanodisks, as all such structures yield considerably high absorption enhancement with the potential of yielding a higher photocurrent upon integration into a standard solar cell stack. Our suggested disordered GRIN metasurface is also promising for thinner solar cells, such as ultrathin c-Si solar cells, for which direct texturing is difficult to accomplish, but antireflection, particularly light trapping, is more crucial.

6. Experimental Section

Sample Fabrication: Details of the fabrication process to produce nanodisk arrays of correlated disorder have been published elsewhere.[27,28] Briefly, it was based on self-organizing colloidal particle deposition onto a functionalized surface. The particle pattern was then exploited as a mask to etch an underlying TiO_2 layer via reactive ion etching (RIE).

The process was started by depositing a 14 nm layer of aluminum oxide (Al_2O_3) onto a c-Si wafer via ALD at 120 °C, using alternating pulses of trimethylaluminium (TMAl) and water (120 each) in a Beneq TFS-200 thermal ALD tool. Then, a TiO_2 layer of 105.5 nm thickness was deposited via ALD at 120 °C using alternating pulses of titanium tetrachloride ($TiCl_4$) and water (1800 pulses each). Furthermore, a 16.8 nm layer of Al_2O_3 was deposited (120 °C, 150 pulses of TMAl and water, each), serving as a functionalization layer for the following particle deposition process. The samples were then exposed to monodisperse aqueous solutions of poly(methyl methacrylate) (PMMA) particles (microParticles Berlin GmbH, Germany) of varying diameter, which formed an evenly distributed disordered arrangement on the surface.[27] The particles were tempered briefly (30 min at 135 °C) for improved coverage of the surface, enabling usage as an etch mask for RIE. The etch process was carried out in two steps: First, the top Al_2O_3 layer was structured into thin nanodisks using a chlorine-containing plasma. In the subsequent fluorine-based process, the structured Al_2O_3 served as a hard-mask to selectively etch the TiO_2 beneath into nanodisks. The bottom Al_2O_3 layer was only weakly etched in fluorine-plasmas and served as an etch-stop layer. Resulting nanodisk arrays are shown, e.g., in Figure 2a,b. The GRIN layer to form the final disordered GRIN metasurface consisted of varying ultrathin layers of ALD deposited Al_2O_3 and TiO_2 (see Section 2.2) using the same respective deposition parameters given above.

Structural Characterization: SEM images were recorded with a field emission microscope (FEI Versa 3D) at 4 kV. Disk diameter and height were evaluated by zoomed-in images of a few particles in the top view and cross-section view, respectively. To extract mean distance $\bar{d}$ and structure factor $S(q)$, disk positions were extracted from images covering an area of at least $80 \times 70\ \mu m^2$ via template matching, i.e., the image of a sample particle was scanned over the image and tested for similarity at every point. Some disk pairs exhibited nominal surface-to-surface distances $\leqslant 0$ nm indicating aggregates and were not considered further. Experimental $S(q)$ was then evaluated using Equation (1).

Optical Characterization: The refractive indices of the deposited thin films were obtained from ellipsometry measurements using a M2000V ellipsometer and the WVASE software (J.A. Woollam Co). The polarization angle was fixed at 45°, and the number of analyzer revolutions to be averaged for each measurement point (revs/meas) was 25. Measurements were carried out at incidence/reflection angles from 60° to 85° in 5° increments and in a wavelength range of $\lambda = 440–1000$ nm in

1.5 nm increments. To fit the gradient layer, the planar Si sample with the 60 nm linear gradient layer was measured. The Cauchy model ($n = A_n + B_n/\lambda^2 + C_n/\lambda^4$) was initially selected and subsequently converted into an effective medium approximation (EMA)-based graded layer. The layer was divided into 12 n-constant sublayers, of which the topmost and the bottom-most layers were fitted. C_n was fixed at zero. The final fit yielded $A_n = 2.272 \pm 0.014$ and $B_n = (8.38 \pm 0.22) \times 10^{-2}\ \mu m^2$ for the bottom layer that corresponded to the values of amorphous TiO_2, and $A_n = 1.6543 \pm 0.0094$ and $B_n = (6.10 \pm 0.88) \cdot 10^{-3}\ \mu m^2$ for the top layer, corresponding to amorphous Al_2O_3.

Specular and diffuse transmittance, T_s and T_d, respectively, as well as reflectance R_s and R_d, respectively, were measured using a PerkinElmer Lambda 950 UV/VIS/NIR spectrophotometer, including an integrating sphere. Experimentally measured absorption amounts to $A = 1 - T_s - T_d - R_s - R_d$.

Supporting Information

Supporting Information is available from the Wiley Online Library or from the author.

Acknowledgements

The authors acknowledge support from Deutsche Forschungsgemeinschaft (DFG) (413644979, RO 3640/11-1 and WE 4051/26-1).

Open access funding enabled and organized by Projekt DEAL.

Conflict of Interest

The authors declare no conflict of interest.

Data Availability Statement

The data that support the findings of this study are available from the corresponding author upon reasonable request.

Keywords

correlated disorder, light trapping, metasurface, solar cell

Received: November 21, 2023
Revised: February 1, 2024
Published online:

[1] F. Berry, R. Mermet-Lyaudoz, J. M. Cuevas Davila, D. A. Djemmah, H. S. Nguyen, C. Seassal, E. Fourmond, C. Chevalier, M. Amara, E. Drouard, *Adv. Energy Mater.* **2022**, *12*, 2200505.

[2] R. Saive, *Prog. Photovolt. Res. Appl.* **2021**, *29*, 1125.
[3] Y. Yao, J. Yao, V. K. Narasimhan, Z. Ruan, C. Xie, S. Fan, Y. Cui, *Nat. Commun.* **2012**, *3*, 664.
[4] M. Otto, M. Algasinger, H. Branz, B. Gesemann, T. Gimpel, K. Füchsel, T. Käsebier, S. Kontermann, S. Koynov, X. Li, V. Naumann, J. Oh, A. N. Sprafke, J. Ziegler, M. Zilk, R. B. Wehrspohn, *Adv. Opt. Mater.* **2015**, *3*, 147.
[5] Z. Fan, D. Cui, Z. Zhang, Z. Zhao, H. Chen, Y. Fan, P. Li, Z. Zhang, C. Xue, S. Yan, *Nanomaterials* **2020**, *11*, 41.
[6] S. Wang, T. Xie, R. Liang, Y. Zhang, F.-J. Ma, D. Payne, G. Scardera, B. Hoex, *ACS Appl. Nano Mater.* **2022**, *5*, 11636.
[7] M. Otto, M. Kroll, T. Käsebier, R. Salzer, A. Tünnermann, R. B. Wehrspohn, *Appl. Phys. Lett.* **2012**, *100*, 191603.
[8] M. Gaudig, J. Hirsch, T. Schneider, A. N. Sprafke, J. Ziegler, N. Bernhard, R. B. Wehrspohn, *J. Vac. Sci. Technol., A* **2015**, *33*, 05E132.
[9] J. N. Munday, H. A. Atwater, *Nano Lett.* **2011**, *11*, 2195.
[10] P. Tillmann, B. Bläsi, S. Burger, M. Hammerschmidt, O. Höhn, C. Becker, K. Jäger, *Opt. Express* **2021**, *29*, 22517.
[11] S. Bhattacharya, I. Baydoun, M. Lin, S. John, *Phys. Rev. Appl.* **2019**, *11*, 014005.
[12] Y. Park, E. Drouard, O. El Daif, X. Letartre, P. Viktorovitch, A. Fave, A. Kaminski, M. Lemiti, C. Seassal, *Opt. Express* **2009**, *17*, 14312.
[13] J. Grandidier, D. M. Callahan, J. N. Munday, H. A. Atwater, *Adv. Mater.* **2011**, *23*, 1272.
[14] Z. Liu, G. Liu, X. Liu, J. Chen, C. Tang, *Opt. Lett.* **2023**, *48*, 1586.
[15] B. Bläsi, M. Hanser, K. Jäger, O. Höhn, *Opt. Express* **2022**, *30*, 24762.
[16] Z. Durmaz, S. Husein, R. Saive, *Opt. Express* **2021**, *29*, 4324.
[17] P. Spinelli, M. Verschuuren, A. Polman, *Nat. Commun.* **2012**, *3*, 692.
[18] P. Spinelli, B. Macco, M. Verschuuren, W. Kessels, A. Polman, *Appl. Phys. Lett.* **2013**, *102*, 23.
[19] C. Zou, P. Gutruf, W. Withayachumnankul, L. Zou, M. Bhaskaran, S. Sriram, C. Fumeaux, *Opt. Lett.* **2016**, *41*, 3391.
[20] E. Slivina, A. Abass, D. Baetzner, B. Strahm, C. Rockstuhl, I. Fernandez-Corbaton, *Phys. Rev. Appl.* **2019**, *12*, 054003.
[21] P. M. Piechulla, E. Slivina, D. Bätzner, I. Fernandez-Corbaton, P. Dhawan, R. B. Wehrspohn, A. N. Sprafke, C. Rockstuhl, *ACS Photonics* **2021**, *8*, 3476.
[22] N. Tavakoli, R. Spalding, A. Lambertz, P. Koppejan, G. Gkantzounis, C. Wan, R. Röhrich, E. Kontoleta, A. F. Koenderink, R. Sapienza, M. Florescu, E. Alarcon-Llado, *ACS Photonics* **2022**, *9*, 1206.
[23] F. Pratesi, M. Burresi, F. Riboli, K. Vynck, D. S. Wiersma, *Opt. Express* **2013**, *21*, A460.
[24] K. Vynck, M. Burresi, F. Riboli, D. S. Wiersma, *Nat. Mater.* **2012**, *11*, 1017.
[25] P. Dhawan, M. Gaudig, A. Sprafke, R. B. Wehrspohn, C. Rockstuhl, *Opt. Express* **2021**, *29*, 19903.
[26] B. Dubrovin, A. Fomenko, S. Novikov, *Modern Geometry–Methods and Applications, Part i, 2nd english ed.*, Springe-Verlag New York Inc.**1992**.
[27] P. M. Piechulla, L. Muehlenbein, R. B. Wehrspohn, S. Nanz, A. Abass, C. Rockstuhl, A. Sprafke, *Adv. Opt. Mater.* **2018**, *6*, 1701272.
[28] P. M. Piechulla, B. Fuhrmann, E. Slivina, C. Rockstuhl, R. B. Wehrspohn, A. N. Sprafke, *Adv. Opt. Mater.* **2021**, *9*, 2100186.
[29] S. Zhong, Y. Zeng, Z. Huang, W. Shen, *Sci. Rep.* **2015**, *5*, 8915.
[30] M. Choi, J. W. Leem, J. S. Yu, *RSC Adv.* **2015**, *5*, 25616.
[31] S.-i. Zaitsu, T. Jitsuno, M. Nakatsuka, T. Yamanaka, S. Motokoshi, *Appl. Phys. Lett.* **2002**, *80*, 2442.
[32] Y. Li, W. Shen, X. Hao, T. Lang, S. Jin, X. Liu, *Appl. Opt.* **2014**, *53*, A270.
[33] W. H. Southwell, *Opt. Lett.* **1983**, *8*, 584.
[34] Y. Zhao, F. Chen, Q. Shen, L. Zhang, *Opt. Express* **2012**, *20*, 11121.
[35] S. Fahr, C. Ulbrich, T. Kirchartz, U. Rau, C. Rockstuhl, F. Lederer, *Opt. Express* **2008**, *16*, 9332.
[36] Z. Ge, P. Rajbhandari, J. Hu, A. Emrani, T. P. Dhakal, C. Westgate, D. Klotzkin, *Appl. Phys. Lett.* **2014**, *104*, 101104.
[37] O. Quevedo-Teruel, W. Tang, R. C. Mitchell-Thomas, A. Dyke, H. Dyke, L. Zhang, S. Haq, Y. Hao, *Sci. Rep.* **2013**, *3*, 1903.
[38] R. Yang, W. Tang, Y. Hao, *Opt. Express* **2011**, *19*, 12348.
[39] L. Liang, S. V. Hum, *Opt. Express* **2013**, *21*, 2133.
[40] P. Kaděra, J. Sánchez-Pastor, H. Eskandari, T. Tyc, M. Sakaki, M. SCHÜßLER, R. Jakoby, N. Benson, A. Jiménez-Sáez, J. Láčík, *IEEE Access* **2022**, *10*, 41097.
[41] P. Dhawan, L. Schulte, P. Piechulla, Y. Augenstein, M. Gaudig, A. Sprafke, R. B. Wehrspohn, C. Rockstuhl, *J. Opt. Soc. Am. B* **2023**, *40*, B8.
[42] O. U. Uche, S. Torquato, F. H. Stillinger, *Phys. Rev. E* **2006**, *74*, 031104.
[43] S. Torquato, O. Uche, F. Stillinger, *Phys. Rev. E* **2006**, *74*, 061308.
[44] T. Akiba, S. Sano, T. Yanase, T. Ohta, M. Koyama, in *Proceedings of the 25th ACM SIGKDD International Conference on knowledge discovery & data mining*, **2019**, pp. 2623–2631.
[45] A. N. Sprafke, R. B. Wehrspohn, *Green* **2012**, *2*, 177.
[46] A. N. Sprafke, R. B. Wehrspohn, in *Photon Management in Solar Cells*, (Eds.: R. B. Wehrspohn, U. Rau, A. Gombert), Wiley-VCH, Weinheim, Germany **2015**, pp. 1–20.
[47] Y. Zhang, M. Nieto-Vesperinas, J. J. Sáenz, *J. Opt.* **2015**, *17*, 105612.